High-resolution surface velocities and strain for Anatolia from Sentinel-1 InSAR and GNSS data

Jonathan R. Weiss[1,2*], Richard J. Walters[3], Yu Morishita[1,4], Tim J. Wright[1], Milan Lazecky[1], Hua Wang[5], Ekbal Hussain[6], Andrew J. Hooper[1], John R. Elliott[1], Chris Rollins[1], Chen Yu[10], Pablo J. González[7,8], Karsten Spaans[9], Zhenhong Li[10], and Barry Parsons[11]

[1]COMET, School of Earth and Environment, University of Leeds, United Kingdom

[2]Institute of Geosciences, University of Potsdam, Germany

[3]COMET, Department of Earth Sciences, University of Durham, United Kingdom

[4]Geospatial Information Authority of Japan, Tsukuba, Japan

[5]Department of Surveying Engineering, Guangdong University of Technology, Guangzhou, China

[6]British Geological Survey, Natural Environment Research Council, United Kingdom

[7]COMET, Department of Earth, Ocean and Ecological Sciences, University of Liverpool, United Kingdom

[8]Volcanology Research Group, Department of Life and Earth Sciences, IPNA-CSIC, Spain

[9]SatSense, Leeds, United Kingdom

[10]COMET, School of Engineering, Newcastle University, United Kingdom

[11]COMET, Department of Earth Sciences, University of Oxford, United Kingdom

*Correspondence to: jonathan.weiss@uni-potsdam.de

Key Points:

- We produce high-resolution horizontal and vertical velocity and strain rate fields for Anatolia from Sentinel-1 and GNSS observations
- Velocity gradients indicate shear strain accumulation along the North and East Anatolian Faults and extension across western Anatolia
- InSAR data are critical for capturing high-resolution details of the velocity and strain rate field

Abstract

Measurements of present-day surface deformation are essential for the assessment of long-term seismic hazard. The European Space Agency's Sentinel-1 radar satellites enable global, high-resolution observation of crustal motion from Interferometric Synthetic Aperture Radar (InSAR). We have developed new automated InSAR processing systems that exploit the first ~5 years of Sentinel-1 data to measure surface motions for the ~800,000 km^2 Anatolian region. Our new 3D velocity and strain rate fields illuminate deformation patterns dominated by westward motion of Anatolia relative to Eurasia, localized strain accumulation along the North and East Anatolian Faults, and rapid vertical signals associated with anthropogenic activities and to a lesser extent extension across the grabens of western Anatolia. We show that automatically processed Sentinel-1 InSAR can characterize details of the velocity and strain rate fields with high resolution and accuracy over large regions. These results are important for assessing the relationship between strain accumulation and release in earthquakes.

Plain Language Summary

Satellite-based measurements of small rates of motion of the Earth's surface made at high spatial resolutions and over large areas are important for many geophysical applications including improving earthquake hazard models. We take advantage of recent advances in satellite-based techniques in order to measure surface velocities and tectonic strain accumulation across the Anatolia region, including the highly seismogenic and often deadly, tectonic-plate bounding North Anatolian Fault. We show that by combining Interferometric Synthetic Aperture Radar (InSAR) data with Global Navigation Satellite System (GNSS) measurements we can enhance our view of surface deformation associated with active tectonics, the earthquake cycle, and anthropogenic processes.

1. Introduction

Geodetic measurements of crustal motion are crucial for understanding the earthquake cycle [e.g. *Elliott et al.*, 2016; *Hearn*, 2003; *Smith and Sandwell*, 2006; *Wright*, 2016; *Wright et al.*, 2001], characterizing spatial variations in lithospheric rheology and fault frictional properties [e.g. *Jolivet et al.*, 2013; *Lindsey et al.*, 2014; *Weiss et al.*, 2019], and illuminating the mechanics of large-scale continental deformation [e.g. *England et al.*, 2016; *Loveless and Meade*, 2011; *Walters et al.*, 2017]. Satellite-based geodetic data are also becoming an increasingly important component of efforts to assess earthquake hazard [e.g. *Chaussard et al.*, 2015; *Kreemer et al.*, 2014] as many major faults exhibit focused and measurable strain at the surface during the interseismic period [*Wei et al.*, 2010; *Wright et al.*, 2004b; *Wright et al.*, 2013].

Geodetic strain rate measurements can be related to seismicity rates [e.g. *Bird et al.*, 2015; *Molnar*, 1979; *Rollins and Avouac*, 2019]. However, global and regional strain rate models usually rely on Global Navigation Satellite System (GNSS) velocity measurements, and these often have insufficient density in many countries at risk from earthquakes, particularly in the Alpine-

Himalayan Belt. Even in well-instrumented regions such as California and Japan, the typical spacing between GNSS observation points of 10-50 km may still be insufficient to resolve strain localization at the scale necessary to distinguish between faults that are locked at the surface and those that are creeping aseismically [*Elliott et al.*, 2016]. The gaps in GNSS coverage are likely to persist and they have a major effect on the corresponding estimates of strain rate; regions of inferred high strain rate are controlled by the distribution of observations, potentially resulting in inaccuracies. Furthermore, temporal variations in strain accumulation around active faults may go undetected if velocities and strain-rate are based on old or non-continuous observations [*Bilham et al.*, 2016; *Cetin et al.*, 2014; *Rousset et al.*, 2016].

Interferometric Synthetic Aperture radar (InSAR) provides spatially continuous measurements of surface motions, without instruments on the ground, with precision approaching that obtained from GNSS, and at a resolution that ranges from meters to hundreds of meters [e.g. *Bürgmann et al.*, 2000; *Hooper et al.*, 2012; *Hussain et al.*, 2016; *Walters et al.*, 2014; *Wright et al.*, 2001]. However, estimating interseismic strain remains challenging particularly in slowly deforming regions where ground displacements are small and error sources can dominate the differential radar phase [*Elliott et al.*, 2016; *Hooper et al.*, 2012; *Shen et al.*, 2019]. Recently, the number of InSAR-capable satellites and volume of associated data have increased and improvements in data quality and processing techniques now permit routine measurements of surface velocities over spatial scales appropriate for studying tectonic plate motions, regional fault systems, and the growth of mountains [e.g. *Fattahi and Amelung*, 2016; *Grandin et al.*, 2012; *Pagli et al.*, 2014; *Tong et al.*, 2013; *Wang and Wright*, 2012; *Wang et al.*, 2019]. In particular, the European Commission's Sentinel-1 constellation, operated by the European Space Agency, with two near-polar orbiting

SAR instruments and a revisit period of 6-12 days for most active tectonic belts, has the potential to be a powerful hazard mapping and monitoring tool, which the geoscience community has begun to exploit [e.g. *Elliott et al.*, 2015; *González et al.*, 2015; *Grandin et al.*, 2016; *Shirzaei et al.*, 2017; *Xu et al.*, 2020]. By analyzing large volumnes of short-revisit Sentinel-1 data, we can produce displacement time series with reduced impact from atmospheric noise.

In order to manage and process the large data volumes produced by Sentinel-1, we have developed open-source, automated workflows to efficiently produce interferograms and line-of-sight (LOS) time series and velocities [*Morishita et al.*, 2020], which are valuable for a range of applications. Here we demonstrate our ability to measure large-scale interseismic deformation across Anatolia, an area encompassing ~800,000 km^2 and including the highly seismogenic North Anatolian Fault (NAF) Zone. We combine InSAR observations from the first ~5 years of the Sentinel-1 mission with published GNSS data to create high-resolution surface velocity and strain rate fields for the region.

2. Sentinel-1 Data and LiCSAR processing

We process Sentinel-1 SAR data acquired on 14 overlapping tracks (7 ascending and 7 descending) over Anatolia, which were selected to cover the entire region from the intersection of the North and East Anatolian Faults in the east to the Aegean Sea in the west (Figs. 1 and S1). Sentinel-1 data were acquired on every 12-day revisit from the beginning of the Sentinel-1A operational mission in October 2014 and every 6 days since Sentinel-1B became fully operational in September 2016.

Our InSAR dataset includes 40 spatially and temporally consistent frames (~250 x 250 km) that we define as part of the Sentinel-1 processing system LiCSAR (Figs. 1 and S1) [*González et al.*, 2016; *Morishita et al.*, 2020]. By default, we construct temporal baseline interferograms to the six closest acquisitions in time (3 forwards and 3 backwards) and ad hoc additional longer-timespan interferograms to help deal with low coherence due to vegetation in summer months and snow cover in winter months. For each frame, this results in a network of ~600-800 interferograms derived from ~200 acquisitions (Fig. S2). Interferograms are downsampled (i.e. multilooked) by a factor of 20 in range and 4 in azimuth producing ground pixels of ~80 x 80 m (resampled to ~100 m spacing during geocoding), and the interferometric phase is unwrapped using a statistical-cost, network-flow algorithm [i.e. SNAPHU; *Chen and Zebker*, 2000; 2001]. We partially mitigate atmospheric contributions to apparent displacement signals by applying the iterative troposphere decomposition model implemented in the Generic Atmospheric Correction Online Service for InSAR (GACOS) [*Yu et al.*, 2017; *Yu et al.*, 2018a; *Yu et al.*, 2018b]. On average GACOS reduces the interferogram phase standard deviations by 20-30% (Fig. S3) [*Morishita et al.*, 2020], which should reduce the uncertainty in our LOS velocities by a similar amount compared to the uncorrected velocities. Additional LiCSAR data processing details can be found in the Supporting Information (SI).

3. Interseismic Line-of-sight Velocity Field Estimation and Uncertainties

We use LiCSBAS, an open-source InSAR time series analysis package integrated with the LiCSAR processing system [*Morishita et al.*, 2020], to derive InSAR LOS displacement time series and velocities. Our LiCSBAS workflow for Anatolia consists of further downsampling the data by a factor of 10 to a pixel size of ~1 km, which is sufficient for large-scale tectonic applications. We perform statistical quality checks [*Morishita et al.*, 2020] prior to the small baseline (SB) inversion, which yields incremental and cumulative displacements and the mean displacement velocity. Despite the short spatial and temporal baselines that generally characterize Sentinel-1 data, gaps in the SB network may still be present due to severe decorrelation (e.g. due to snowfall), extended periods of time with no acquisitions, and after unwrapping consistency checks (Fig. S2). LiCSBAS circumvents this problem by imposing the constraint that displacements are linear in time (i.e. constant velocity) across the gaps [e.g. *Doin et al.*, 2011; *López-Quiroz et al.*, 2009]. Finally, we estimate the uncertainty in the velocity from its standard deviation (STD) using the percentile bootstrap method [*Efron and Tibshirani*, 1986] (Fig. S4) and we mask pixels based on several noise indices (Fig. S5). We also test for potential velocity biases associated with short temporal baseline interferograms in a Sentinel-1 network [e.g. *Ansari et al.*, 2020] by removing 6- and 12-day pairs for one LiCSAR frame prior to LiCSBAS velocity inversion (Fig. S11); the standard deviation of the difference between these results is small (~2 mm/yr).

After LiCSAR/LiCSBAS processing each frame has its own independent reference point for velocity determination (e.g. Fig. S6). We transform the LOS rate maps into a Eurasia-fixed reference frame using a regional GNSS velocity compilation (Fig. 1A and SI) following the method outlined in *Hussain et al.* [2018]; for each frame, we estimate and remove the best-fitting second order polynomial between an interpolated, smoothed GNSS-derived horizontal velocity field projected into the satellite LOS and the InSAR velocities (Fig. 1; SI). This transformation yields a velocity field where the longest wavelength signals are tied to the GNSS data, but it does not affect features at the ~100 km length scale and below.

Fault-perpendicular profiles from the overlap zones of adjacent tracks provide an indication of how well the rate maps agree after the reference frame transformation (Fig. 2). We present one profile taken from ascending-track data crossing the NAF near Ismetpasa and extending southward through the Konya Basin (Figs. 1 and 2) and another taken farther east from descending-track data crossing the NAF and EAF. Both profiles show good agreement between adjacent frames and clear changes in LOS velocity across major fault zones, consistent with the localization of interseismic strain [*Cavalié and Jónsson*, 2014; *Walters et al.*, 2014].

The bootstrap-derived uncertainties are generally considered to be underestimates particularly if the network is not fully connected [*Morishita et al.*, 2020]. Therefore, we also assess LOS velocity uncertainties by calculating the difference between our LOS velocities and a velocity field created by interpolating horizontal GNSS data (see SI), and an associated semi-variogram γ at separation distances h ranging from 0 to 150 km for two off-fault frames (Fig. S6). Our $\sqrt{\gamma(h)}$ values serve as an estimate of velocity uncertainty that is robust up to length scales of ~150 km (see SI) [*Bagnardi and Hooper*, 2018]. We use this approach to examine the evolution of uncertainty in our residual LOS measurements by estimating $\sqrt{\gamma(h)}$ for progressively longer time intervals and we find general consistency with the theoretical model derived for error analysis of GNSS time-series data [*Zhang et al.*, 1997] for the first ~3 years of our Sentinel-1 time series (Fig. S6). At longer time intervals the uncertainty estimates on our Eurasia-fixed velocity estimates reach a minimum of 2-3 mm/yr, likely because our interpolated GNSS velocities are only accurate to this level, whereas the bootstrap-derived estimates continue to decrease with increasing time series length. However, this exercise is useful for determining our ability to measure small amounts of displacement, the time necessary to achieve a certain level of accuracy across different length scales [*Morishita et al.*, 2020], and how detection limits on interseismic velocities evolve with time (Fig. S6).

As an additional estimate of uncertainty, we also calculate the velocity residuals in the overlap areas for all frames. We do this by assuming horizontal motion only and by correcting for variable LOS by dividing the LOS velocities by the sine of the local incidence angles before multiplying by the sine of the incidence angle at the center of each track [e.g. *Hussain et al.*, 2018; *Walters et al.*, 2014]. Histograms of the overlap residuals are approximately Gaussian with means close to zero and standard deviations of 3.1-3.7 mm/yr (Fig. S7). Because LOS velocities are not purely horizontal and due to uncertainties in the GNSS velocities used to transform the LOS information into a Eurasia-fixed reference frame, these values can be considered upper-bound estimates of $\sqrt{2} \times$ the velocity uncertainties for the frames giving an average LOS velocity STD of ~2.4 mm/yr.

4. East-west and Vertical Surface Velocities for Anatolia

The Eurasia-fixed ascending and descending LOS velocities (Fig. 1) provide a detailed picture of Anatolian surface motions. The most prominent feature is the pronounced gradient in velocity across the NAF, from negligible motion north of the NAF to rapid westward motion of Anatolia relative to Eurasia south of the fault (e.g. Fig. S6). Additional features include localized regions where there is apparent motion away from the satellite in both ascending and descending geometries indicating subsidence (Fig. 1B, 1C, and S6).

To remove some of the ambiguity associated with LOS measurements, we follow the approach of *Wright et al.* [2004a] and decompose the LOS velocities into east-west and vertical components for pixels with both ascending and descending information

$$V_{LOS} = [sin\,\theta\,cos\,\alpha \quad -sin\,\theta\,sin\,\alpha \quad -cos\,\theta] \begin{bmatrix} V_E \\ V_N \\ V_U \end{bmatrix}$$

where V_{LOS} is the Eurasia-fixed LOS velocity, θ is the local radar incidence angle, α is the azimuth of the satellite heading vector, and $[V_E\ V_N\ V_U]^T$ is a vector with the east, north, and vertical components of motion, respectively. This equation has three unknowns and we have two observational constraints in the form of ascending and descending LOS velocities. To calculate the full 3-D velocity field, we note that both viewing geometries are relatively insensitive to north-south motion and use the interpolated, smoothed north-south component of the GNSS velocity field (Fig. 3A) to constrain V_N before solving for V_E and V_U. This approach does not result in smoothed east-west or vertical velocities because of the LOS north-south insensitivity.

The resulting decomposed east-west velocity field (Fig. 3) is easier to interpret than the LOS rate map mosaic and shows large-scale westward motion of Anatolia at a rate of 20-25 mm/yr relative to Eurasia, with visible strain (a localized velocity gradient) across the entire NAF and portions of the EAF (Fig. 3B). Along-strike variations in the width of the velocity transition are also evident and correspond to portions of the NAF near Izmit and Ismetpasa where shallow aseismic slip (i.e. creep) has been previously documented (Figs. 1, 3, and S9) [*Ambraseys*, 1970; *Bilham et al.*, 2016; *Cakir et al.*, 2014; *Hussain et al.*, 2016; *Jolivet and Frank*, 2020; *Kaneko et al.*, 2013; *Rousset et al.*, 2016].

The decomposed velocity field reveals that portions of Anatolia are experiencing rapid vertical motions. The clearest example is the large zone of subsidence with rates >50 mm/yr surrounding the Konya Basin in south-central Turkey (Figs. 2A, 3C, 3E, S6, and S11), which is attributed to rapid aquifer compaction due to groundwater extraction [*Caló et al.*, 2017; *Üstün et al.*, 2015].

5. Velocity and Strain Rate Fields from Sentinel-1 InSAR and GNSS Data

To estimate rates of tectonic strain accumulation, we can calculate velocity gradients directly from the decomposed velocity field (see SI; Fig. S10) but our preferred method (see SI for a detailed justification) involves combining InSAR LOS velocity maps with GNSS data and inverting for a velocity and strain rate model using the VELMAP approach [*Wang and Wright*, 2012] (see SI). The technique consists of dividing the study area into a mesh of arbitrary spherical triangles (Fig. S13), assuming the velocity varies linearly (i.e. the strain rate is constant) within each triangle, and using shape functions [*England and Molnar*, 2005] to solve for the unknown velocities at the vertices of each triangle using the observed InSAR and GNSS measurements. The associated strain and rotation rates are calculated using the spherical approximation equations of *Savage et al.* [2001]. The inversion is regularized using Laplacian smoothing, the strength of which has an impact on the resulting strain rate magnitudes (Figs. S13 and S15) including slightly underestimating the strain rates associated with active faults. The approach also does not allow for steps in the velocity field. Additional VELMAP modeling information can be found in the SI.

Comparison of our preferred Sentinel-1- and GNSS-based model with one based on GNSS data alone (see SI; Figs. 4 and S15) reveals that the inclusion of InSAR data improves the accuracy of the velocity field and better captures velocity gradients (and therefore also estimates of strain accumulation) along the major faults (Fig. 2). In the GNSS-only model, the second invariant of the horizontal components of the strain rate tensor (a measure of the total magnitude of the strain rate) indicates the NAF is characterized by a patchy distribution of regions straining at rates >100 nanostrain/yr with even higher strain rates (≥150 nanostrain/yr) primarily near clusters of GNSS sites around the western and eastern strands of the fault. Furthermore, central Anatolia is inferred to be essentially undeforming, but in Western Anatolia where earthquake focal mechanisms and the GPS-derived velocity and strain rate fields of *Aktug et al.* [2009] show that normal faulting and extension is prevalent, portions of the major grabens are straining at rates >50 nanostrain/yr (Figs. 3 and 4). In contrast, the combined InSAR and GNSS strain rate model shows spatially coherent strain rate magnitudes ≥150 nanostrain/yr localized along nearly the entire length of the NAF. The previously identified creeping sections of the fault (Fig. 2B) are also associated with elevated strain rates compared to the GNSS-only map, which exhibits high strain rates in the Izmit region (Fig. 2D) but much lower rates near Ismetpasa (Fig. S9). For comparison, we also derive VELMAP strain rates using the alternative Global Strain Rate Model (GSRM) GNSS dataset [see SI; *Kreemer et al.*, 2014], which are characterized by localized patches of high strain along the NAF and in central Anatolia, largely controlled by GNSS site density (Fig. S17).

Another characteristic of our combined Sentinel-1 InSAR and GNSS result is that the inferred strain rates along the NAF (Fig. 4) are typically half of those stemming from an analysis of Envisat InSAR data by *Hussain et al.* [2018], who took a different approach to estimating strain rate by modeling fault-parallel velocities using 1-D elastic dislocation theory. A main conclusion of *Hussain et al.* [2018] is that strain rates are essentially uniform along the entire length of the fault, implying that the interseismic strain rate is constant in time except in the first decade or two after a major earthquake. We attribute most of the strain rate magnitude discrepancy to the factor of two difference between shear strain rates obtained by computing the full strain rate tensor [*Savage and Burford*, 1973; *Savage et al.*, 2001] and those obtained by taking the spatial derivative of the smoothed, decomposed east-west surface velocity field (i.e. the velocity gradient; Fig. S10; see SI for a detailed explanation) or as in *Hussain et al.* [2018], the gradient of fault-parallel velocity profiles associated with slip on a dislocation in an elastic half space. Once the factor of two is taken in to account, our strain rate magnitudes are still slightly lower than those of *Hussain et al.* [2018] but exhibit a similar first-order pattern suggesting the nearly constant along-strike strain rate is a real and robust feature of the NAF (Fig. S19). This result has important implications as it suggests geodetic strain rate can be used as a long-term estimate of future seismic hazard independent of time since the last earthquake. Second-order differences in strain rate magnitudes are due to the smoothing implemented in VELMAP (Figs. S13, S15, and S19) and not explicitly accounting for fault creep. For example, if we examine the NAF-parallel velocities in a profile that crosses the creeping zone near Ismetpasa, we see that our preferred solution does not capture the sharp velocity gradient evident in the GSRM GNSS velocities (Fig. 2B). Rougher VELMAP models (e.g. Figs. S15 and S16) better reproduce this gradient and return strain rate magnitudes more consistent with the dislocation-based estimates of *Hussain et al.* [2018], but also introduce unacceptably high levels of apparent noise in the central Anatolian strain field (e.g. Fig. S15). Future efforts will focus on developing an improved approach to model regularization that includes spatially variable smoothing and accounts for fault creep.

While a velocity gradient across portions of the EAF is visible in the decomposed east-west velocities (Fig. 3), our combined strain rate model infers relatively low levels of strain along this fault zone compared to the NAF (Fig. 4), consistent with previous InSAR-based studies [e.g. *Cavalié and Jónsson*, 2014; *Walters et al.*, 2014]. Furthermore, we find appreciable, localized strain accumulation only along the northeastern half of the EAF that is not apparent in the GNSS-only model. This is also where the east-west velocity contrast is most apparent (Fig. 3B). While there is some seismicity associated with the EAF (Fig. 3A), the recently complied 1900-2012 earthquake catalogue for Turkey [*Kadirioğlu et al.*, 2018] indicates that the associated magnitudes and thus total moment release are much lower than along the NAF, supporting the notion that less strain is accumulating along the EAF than the NAF [*Bletery et al.*, 2020]. The 24 January 2020 M_w 6.7 Elaziğ earthquake [*Melgar et al.*, 2020] occurred on the short portion of the EAF where we resolve both an east-west velocity gradient and elevated strain rates on the order of ~70 nanostrain/yr (Figs. 3 and 4). We infer maximum shear strain and dilatation rates ≥100 nanostrain/yr associated with active grabens and normal faulting within a broad zone of positive dilatation across the Western Anatolian Extensional Province but relatively low levels of strain along the Central Anatolian Fault Zone (Figs. 3 and 4).

6. Conclusions

We have produced, to our knowledge, the largest regional interseismic measurement from InSAR to date, covering a ~800,000 km^2 area and the majority of Anatolia. Our strain rate model displays high strains along the major tectonic features, which is consistent with the distribution of seismicity (Figs. 2A and S20). While the availability of abundant GNSS and Sentinel-1 InSAR data for Anatolia combined with favorable fault orientations make it ideal for such a study, our results demonstrate the potential of Sentinel-1 data for enhancing the picture of surface deformation and hazard in other regions. A key factor is the equal geographical coverage of Sentinel-1 ascending and descending data, which permits the retrieval of 2D and 3D deformation fields for tectonic zones globally even without the benefit of a dense GNSS dataset (see SI; Fig. S19. In addition, the relatively low uncertainties on Sentinel-1-derived interseismic velocities (Fig. S7) are beneficial for estimating strain across slowly deforming regions and for resolving small temporal changes in deformation throughout the earthquake cycle. Although some challenges still remain for fault systems where the majority of motion is in the north-south direction, Sentinel-1 represents a major improvement over past SAR datasets. This improvement is crucial for monitoring vertical motions from anthropogenic activities and for constraining earthquake hazard, particularly across regions with millennial earthquake recurrence intervals, where seismic hazard assessments based on incomplete historical earthquake records can dangerously underestimate the true hazard [*Stein et al.*, 2012; *Stevens and Avouac*, 2016].

Acknowledgements

We thank Marco Bagnardi and Thomas Ingleby for helping JRW get up to speed with InSAR upon his arrival in Leeds, Philip England and Gregory Houseman for insights regarding deriving velocities and strain rates from geodetic data, and Emma Hatton and Nicholas Greenall for their contributions to LiCSAR development. We also thank Romain Jolivet, Lucy Flesch, and an anonymous reviewer for comments that helped us improve the manuscript. We are grateful to Tom Merry for help with code debugging. This research was supported by the Natural Environmental Research Council (NERC) through the Centre for the Observation and Modelling of Earthquakes, Volcanoes and Tectonics, the Looking inside the Continents from Space large grants to Oxford

(NE/K011006/1), Leeds (NE/K010867/1), and Newcastle (NE/K010794/1) Universities, and the Earthquakes without Frontiers project (EwF_NE/J02001X/1_1). JRW is also supported by the German Research Foundation (DFG) and the State of Brandenburg, TJW by the Royal Society, YM by the Japan Society for the Promotion of Science Overseas Research Fellowship, and HW by the NSFC (41672205). GMT [*Wessel et al.*, 2013] was used to create the figures presented in this paper. All interferograms are available for download from comet.nerc.ac.uk/comet-lics-portal, the time series analysis software is available from github.com/yumorishita/LiCSBAS, and GACOS corrections can be requested from ceg-research.ncl.ac.uk/v2/gacos.

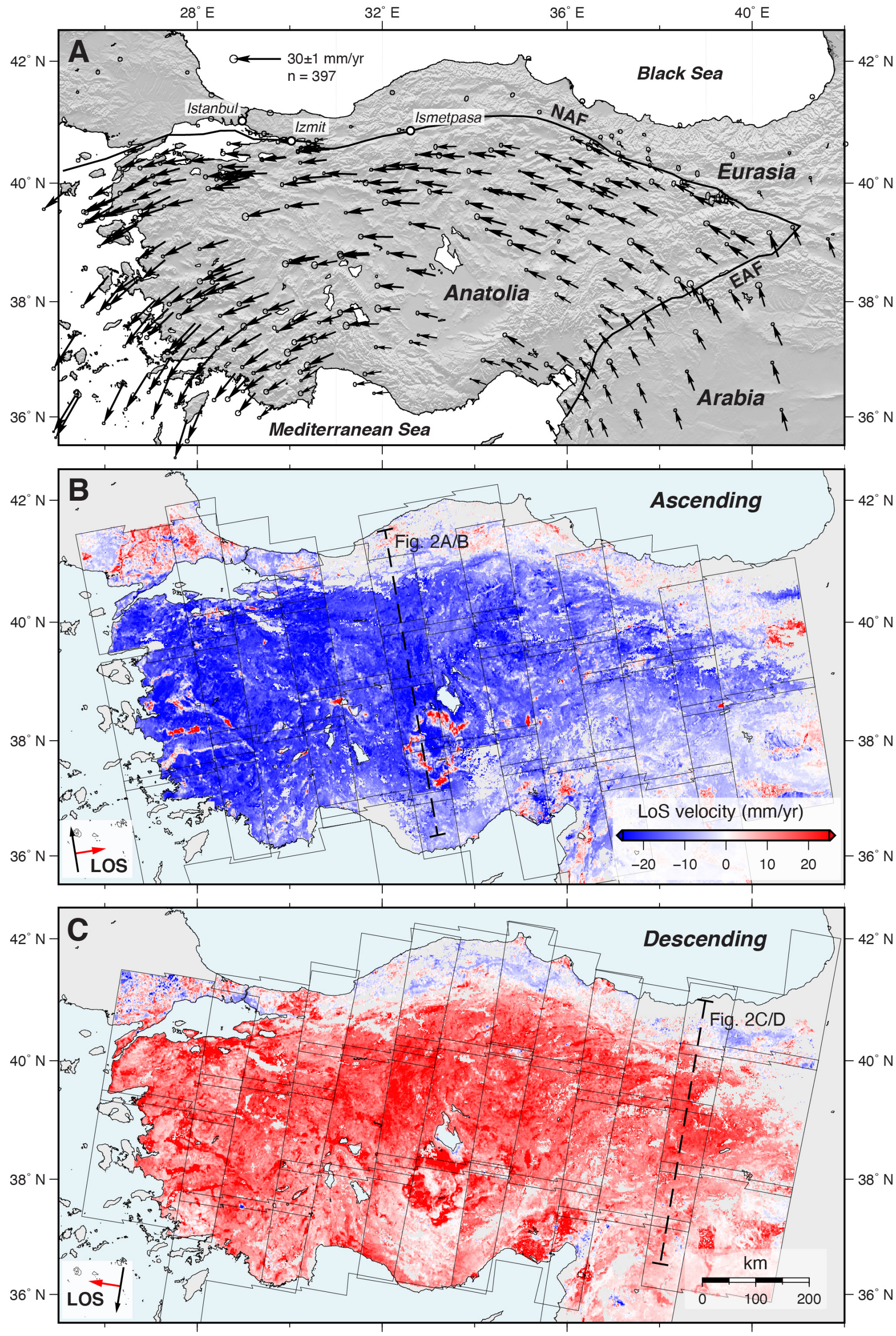

Fig. 1. Tectonic setting of Anatolia and interseismic surface velocities in a Eurasia-fixed reference frame. (A) GNSS velocity vectors from *England et al.* [2016] and *Nocquet* [2012], illuminating the counterclockwise rotation of Anatolia and Arabia relative to Eurasia. Black lines indicate the main strands of the North Anatolian Fault (NAF) and East Anatolian Fault (EAF). (B) Ascending and (C) descending track Sentinel-1 line-of-sight (LOS) velocities with LiCSAR frame boundaries. Negative (blue) and positive (red) values indicate relative motion towards and away from the satellite, respectively. Color scale is the same in (B) and (C). Fig. 2 profile locations are indicated in (B) and (C).

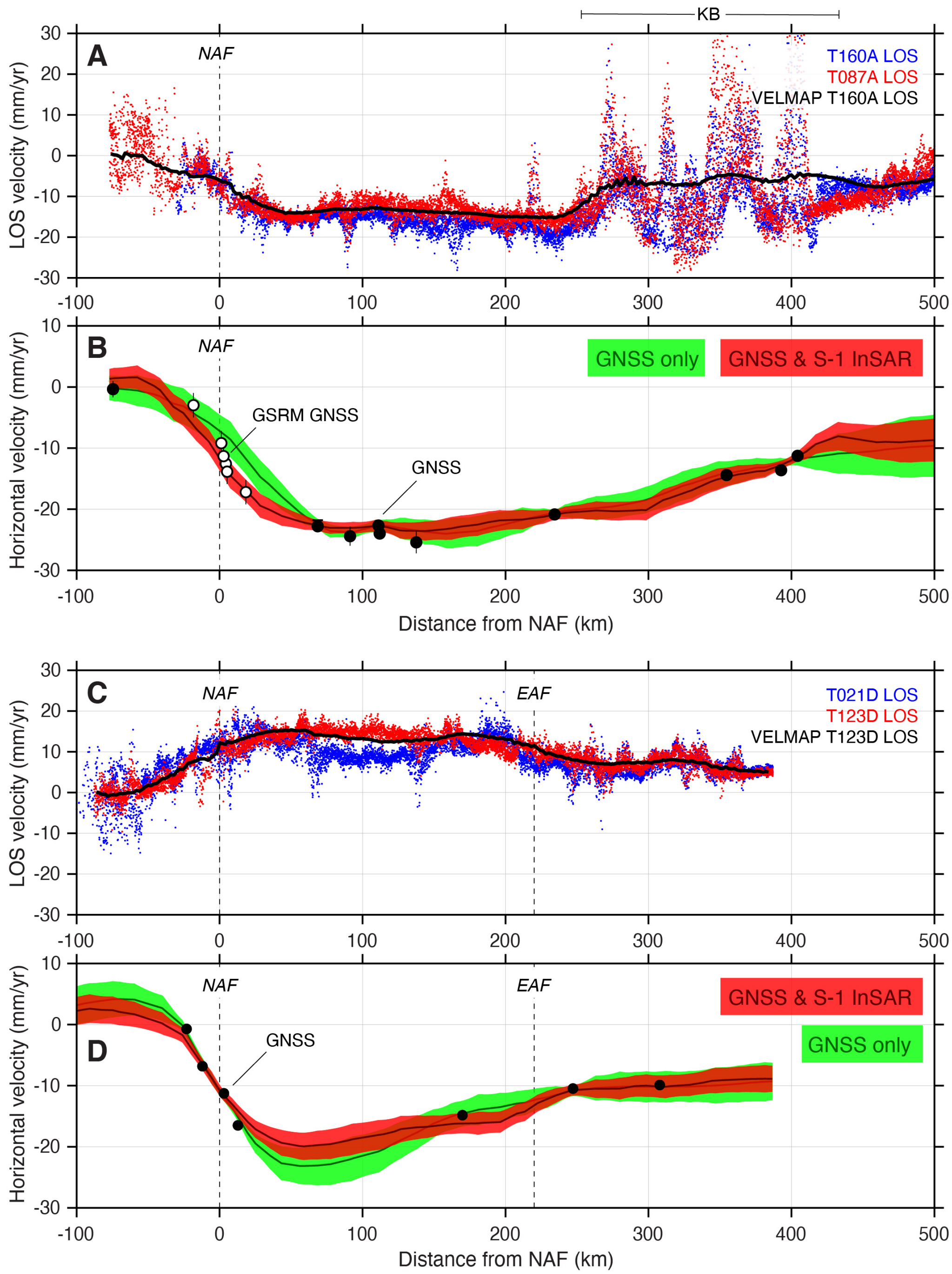

Fig. 2. Velocity profiles for Anatolia. (A) InSAR LOS velocities within 25 km of the NAF-crossing profile shown in Fig. 1B for overlapping tracks T160A (blue) and T087A (red). The black line is the mean VELMAP LOS velocity for T087A. (B) Red band shows combined Sentinel-1 InSAR and GNSS profile-perpendicular horizontal velocities with 1σ errors from our preferred VELMAP model. Green band represents the GNSS-only model. Filled circles and 2σ error bars are the GNSS velocities (white from GSRM are not used in the VELMAP inversion). The southern portion of the profile crosses the Konya Basin (KB; see main text and Fig. S8). (C-D) Same as above but for a profile that crosses the NAF and EAF (Fig. 1C).

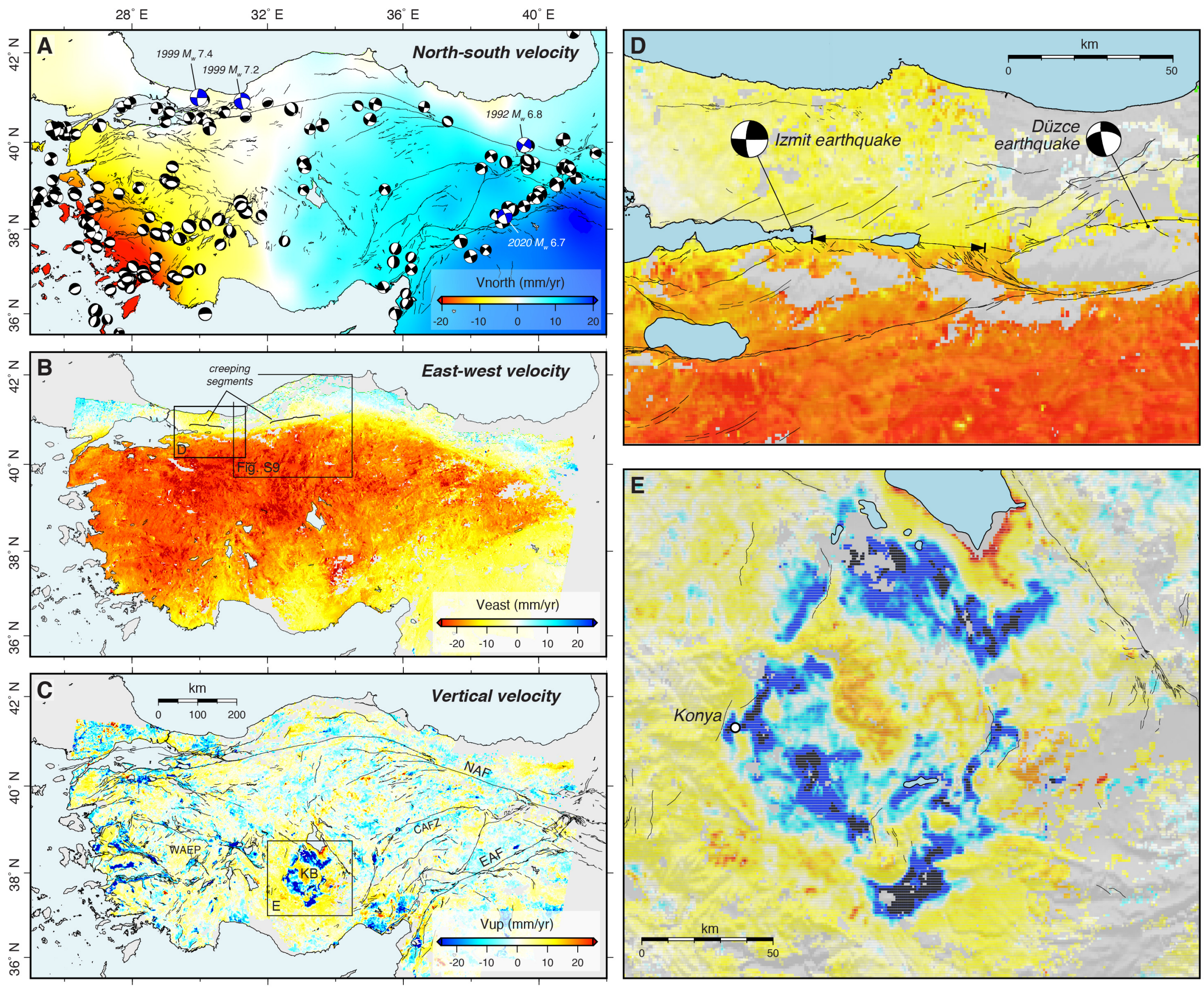

Fig. 3. Horizontal and vertical surface velocities for the Anatolian region. (A) Interpolated north-south velocities based on the GNSS data and shallow earthquake focal mechanisms from the GCMT catalogue [*Ekström et al.*, 2012]. Recent large labeled events include the 1999 M_w 7.4 Izmit, the 1999 M_w 7.2 Düzce, the 1992 M_w 6.8 Erzincan, and the 2020 M_w 6.7 Elaziğ earthquakes. (B) East-west and (C) vertical velocities decomposed from the combined Sentinel-1 LOS and GNSS north-south velocities. Previously identified creeping portions of the NAF are indicated in (B). Also shown are close-up views of the decomposed surface velocities for (D) a section of the NAF surrounding the Izmit and Düzce earthquakes with the creeping section determined by *Aslan et al.* [2019] indicated with arrows and (E) the Konya Basin region with areas subsiding at rates ≥50 mm/yr shown in black. Semi-transparent SRTM topography hill-shades are draped over the velocity fields shown in the close-ups. See Fig. S9 for a detailed view of the creeping section near Ismetpasa. Thin black lines in (A), (C), (D), and (E) are active faults from [*Emre et al.*, 2018]. KB=Konya Basin. CAFZ=Central Anatolian Fault Zone. WAEP=Western Anatolian Extensional Province.

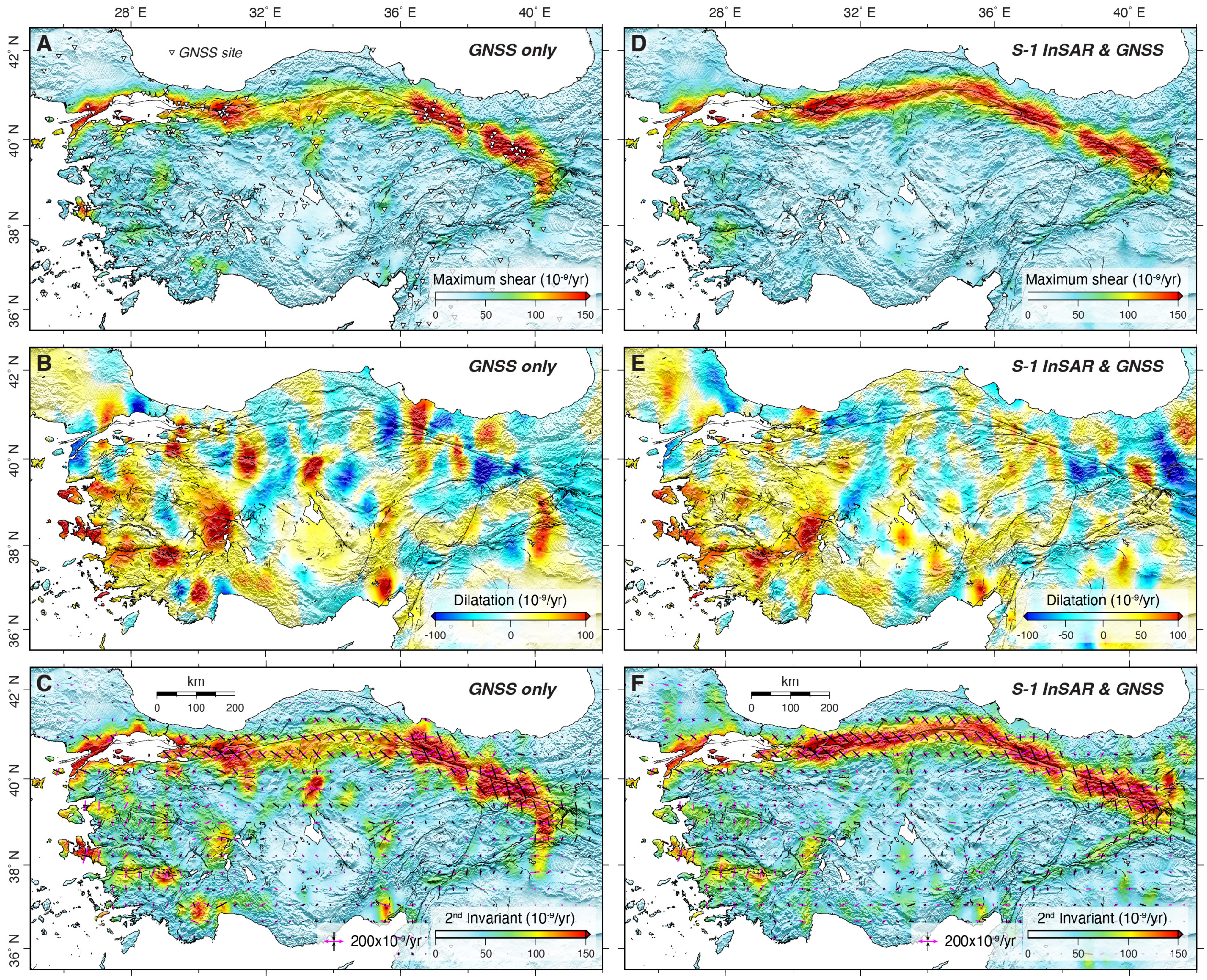

Fig. 4 VELMAP strain rate fields for Anatolia. (A) Maximum shear strain rate, (B) dilatation rate, and (C) second invariant of the strain rate tensor, derived using GNSS data only. White triangles in (A) are GNSS site locations. (D-F) Strain rate components from a joint inversion of the GNSS and Sentinel-1 LOS velocities. Black and magenta bars in (C) and (F) represent the contractional and extensional principal strain rates, respectively. The maximum shear strain rates imply focused deformation along the NAF and EAF and wholesale positive dilatation across western Anatolia is indicative of extension whereas short-wavelength features in the dilatation field likely reflect anthropogenic vertical signals that result in subsurface expansion and contraction and contribute to noisy patches in the 2nd invariant estimates. See Figs. S15 and S19 for additional components of the strain rate tensor and a comparison with seismicity rates, respectively.

References

Aktug, B., et al. (2009), Deformation of western Turkey from a combination of permanent and campaign GPS data: Limits to block-like behavior, *Journal of Geophysical Research: Solid Earth*, *114*(B10).

Ambraseys, N. N. (1970), Some characteristic features of the Anatolian fault zone, *Tectonophysics*, *9*(2), 143-165.

Ansari, H., F. De Zan, and A. Parizzi (2020), *Study of Systematic Bias in Measuring Surface Deformation with SAR Interferometry*.

Argus, D. F., R. G. Gordon, and C. DeMets (2011), Geologically current motion of 56 plates relative to the no-net-rotation reference frame, *Geochemistry, Geophysics, Geosystems*, *12*(11).

Aslan, G., C. Lasserre, Z. Cakir, S. Ergintav, S. Özarpaci, U. Dogan, R. Bilham, and F. Renard (2019), Shallow Creep Along the 1999 Izmit Earthquake Rupture (Turkey) From GPS and High Temporal Resolution Interferometric Synthetic Aperture Radar Data (2011–2017), *Journal of Geophysical Research: Solid Earth*, *124*(2), 2218-2236.

Bagnardi, M., and A. Hooper (2018), Inversion of Surface Deformation Data for Rapid Estimates of Source Parameters and Uncertainties: A Bayesian Approach, *Geochemistry, Geophysics, Geosystems*, *19*(7), 2194-2211.

Bilham, R., et al. (2016), Surface creep on the North Anatolian Fault at Ismetpasa, Turkey, 1944–2016, *Journal of Geophysical Research: Solid Earth*, *121*(10), 7409-7431.

Bird, P., D. D. Jackson, Y. Y. Kagan, C. Kreemer, and R. S. Stein (2015), GEAR1: A Global Earthquake Activity Rate Model Constructed from Geodetic Strain Rates and Smoothed Seismicity, *Bulletin of the Seismological Society of America*.

Bletery, Q., O. Cavalie, J.-M. Nocquet, and T. Ragon (2020), Distribution of interseismic coupling along the North and East Anatolian Faults inferred from InSAR and GPS data, *Earth and Space Science Open Archive*.

Bürgmann, R., P. A. Rosen, and E. J. Fielding (2000), Synthetic Aperture Radar Interferometry to Measure Earth's Surface Topography and Its Deformation, *Annual Review of Earth and Planetary Sciences*, *28*(1), 169-209.

Cakir, Z., S. Ergintav, A. M. Akoğlu, R. Çakmak, O. Tatar, and M. Meghraoui (2014), InSAR velocity field across the North Anatolian Fault (eastern Turkey): Implications for the loading and release of interseismic strain accumulation, *Journal of Geophysical Research: Solid Earth*, *119*(10), 7934-7943.

Caló, F., D. Notti, J. P. Galve, S. Abdikan, T. Görüm, A. Pepe, and F. Balik Şanli (2017), DInSAR-Based Detection of Land Subsidence and Correlation with Groundwater Depletion in Konya Plain, Turkey, *Remote Sensing*, *9*(1), 83.

Cavalié, O., and S. Jónsson (2014), Block-like plate movements in eastern Anatolia observed by InSAR, *Geophysical Research Letters*, *41*(1), 26-31.

Cetin, E., Z. Cakir, M. Meghraoui, S. Ergintav, and A. M. Akoglu (2014), Extent and distribution of aseismic slip on the Ismetpaşa segment of the North Anatolian Fault (Turkey) from Persistent Scatterer InSAR, *Geochemistry, Geophysics, Geosystems*, *15*(7), 2883-2894.

Chaussard, E., R. Bürgmann, H. Fattahi, R. M. Nadeau, T. Taira, C. W. Johnson, and I. Johanson (2015), Potential for larger earthquakes in the East San Francisco Bay Area due to the direct connection between the Hayward and Calaveras Faults, *Geophysical Research Letters*, *42*(8), 2734-2741.

Chen, C. W., and H. A. Zebker (2000), Network approaches to two-dimensional phase unwrapping: intractability and two new algorithms, *J. Opt. Soc. Am. A*, *17*(3), 401-414.

Chen, C. W., and H. A. Zebker (2001), Two-dimensional phase unwrapping with use of statistical models for cost functions in nonlinear optimization, *J. Opt. Soc. Am. A*, *18*(2), 338-351.

Doin, M.-P., F. Lodge, S. Guillaso, R. Jolivet, C. Lasserre, G. Ducret, R. Grandin, E. Pathier, and V. Pinel (2011), Presentation of the small baseline NSBAS processing chain on a case example: The Etna deformation monitoring from 2003 to 2010 using Envisat data, in *FRINGE*, edited, Frascati, Italy.

Efron, B., and R. Tibshirani (1986), Bootstrap Methods for Standard Errors, Confidence Intervals, and Other Measures of Statistical Accuracy, *Statist. Sci.*, *1*(1), 54-75.

Ekström, G., M. Nettles, and A. M. Dziewoński (2012), The global CMT project 2004–2010: Centroid-moment tensors for 13,017 earthquakes, *Physics of the Earth and Planetary Interiors*, *200-201*, 1-9.

Elliott, J. R., R. J. Walters, and T. J. Wright (2016), The role of space-based observation in understanding and responding to active tectonics and earthquakes, *Nature Communications*, *7*, 13844.

Elliott, J. R., A. J. Elliott, A. Hooper, Y. Larsen, P. Marinkovic, and T. J. Wright (2015), Earthquake monitoring gets boost from new satellite, *Eos, Transactions American Geophysical Union*, *96*.

Emre, Ö., T. Y. Duman, S. Özalp, F. Şaroğlu, Ş. Olgun, H. Elmacı, and T. Çan (2018), Active fault database of Turkey, *Bulletin of Earthquake Engineering*, *16*(8), 3229-3275.

England, P., and P. Molnar (2005), Late Quaternary to decadal velocity fields in Asia, *Journal of Geophysical Research: Solid Earth*, *110*(B12), n/a-n/a.

England, P. C., G. A. Houseman, and J. M. Nocquet (2016), Constraints from GPS measurements on the dynamics of deformation in Anatolia and the Aegean, *Journal of Geophysical Research: Solid Earth*.

Fattahi, H., and F. Amelung (2016), InSAR observations of strain accumulation and fault creep along the Chaman Fault system, Pakistan and Afghanistan, *Geophysical Research Letters*, *43*(16), 8399-8406.

Goldstein, R. M., and C. L. Werner (1998), Radar interferogram filtering for geophysical applications, *Geophysical Research Letters*, *25*(21), 4035-4038.

González, P. J., E. Hatton, R. J. Walters, A. J. Hooper, and T. J. Wright (2016), Sentinel-1 InSAR time series processing: one year and counting, paper presented at The Living Planet Symposium, Czech Republic.

González, P. J., M. Bagnardi, A. J. Hooper, Y. Larsen, P. Marinkovic, S. V. Samsonov, and T. J. Wright (2015), The 2014–2015 eruption of Fogo volcano: Geodetic modeling of Sentinel-1 TOPS interferometry, *Geophysical Research Letters*, *42*(21), 9239-9246.

Grandin, R., E. Klein, M. Métois, and C. Vigny (2016), Three-dimensional displacement field of the 2015 Mw8.3 Illapel earthquake (Chile) from across- and along-track Sentinel-1 TOPS interferometry, *Geophysical Research Letters*, *43*(6), 2552-2561.

Grandin, R., M.-P. Doin, L. Bollinger, B. Pinel-Puyssegu, G. Ducret, R. Jolivet, and S. N. Sapkota (2012), Long-term growth of the Himalaya inferred from interseismic InSAR measurement, *Geology*, *40*(12), 1059-1062.

Hearn, E. H. (2003), What can GPS data tell us about the dynamics of post-seismic deformation?, *Geophysical Journal International*, *155*(3), 753-777.

Hooper, A., D. Bekaert, K. Spaans, and M. Arıkan (2012), Recent advances in SAR interferometry time series analysis for measuring crustal deformation, *Tectonophysics*, *514-517*, 1-13.

Hussain, E., A. Hooper, T. J. Wright, R. J. Walters, and D. P. S. Bekaert (2016), Interseismic strain accumulation across the central North Anatolian Fault from iteratively unwrapped InSAR measurements, *Journal of Geophysical Research: Solid Earth*, *121*(12), 9000-9019.

Hussain, E., T. J. Wright, R. J. Walters, D. P. S. Bekaert, R. Lloyd, and A. Hooper (2018), Constant strain accumulation rate between major earthquakes on the North Anatolian Fault, *Nature Communications*, *9*(1), 1392.

Jolivet, R., and W. B. Frank (2020), The Transient and Intermittent Nature of Slow Slip, *AGU Advances*, *1*(1), e2019AV000126.

Jolivet, R., C. Lasserre, M. P. Doin, G. Peltzer, J. P. Avouac, J. Sun, and R. Dailu (2013), Spatio-temporal evolution of aseismic slip along the Haiyuan fault, China: Implications for fault frictional properties, *Earth and Planetary Science Letters*, *377-378*, 23-33.

Kadirioğlu, F., R. Kartal, T. Kılıç, D. Kalafat, T. Duman, T. Eroğlu Azak, S. Özalp, and Ö. Emre (2018), An improved earthquake catalogue ($M \geq 4.0$) for Turkey and its near vicinity (1900–2012), *Bulletin of Earthquake Engineering*, *16*, 3317-3338.

Kaneko, Y., Y. Fialko, D. T. Sandwell, X. Tong, and M. Furuya (2013), Interseismic deformation and creep along the central section of the North Anatolian Fault (Turkey): InSAR observations and implications for rate-and-state friction properties, *Journal of Geophysical Research: Solid Earth*, *118*(1), 316-331.

Kreemer, C., G. Blewitt, and E. C. Klein (2014), A geodetic plate motion and Global Strain Rate Model, *Geochemistry, Geophysics, Geosystems*, *15*(10), 3849-3889.

Lindsey, E. O., Y. Fialko, Y. Bock, D. T. Sandwell, and R. Bilham (2014), Localized and distributed creep along the southern San Andreas Fault, *Journal of Geophysical Research: Solid Earth*, *119*(10), 7909-7922.

López-Quiroz, P., M.-P. Doin, F. Tupin, P. Briole, and J.-M. Nicolas (2009), Time series analysis of Mexico City subsidence constrained by radar interferometry, *Journal of Applied Geophysics*, *69*(1), 1-15.

Loveless, J. P., and B. J. Meade (2011), Partitioning of localized and diffuse deformation in the Tibetan Plateau from joint inversions of geologic and geodetic observations, *Earth and Planetary Science Letters*, *303*(1), 11-24.

Melgar, D., A. Ganas, T. Taymaz, S. Valkaniotis, B. W. Crowell, V. Kapetanidis, V. Tsironi, S. Yolsal-Cevikbilen, and T. Ocalan (2020), Rupture Kinematics of January 24, 2020 Mw 6.7 Doğanyol-Sivrice, Turkey Earthquake on the East Anatolian Fault Zone Imaged by Space Geodesy, *EarthArXiv*.

Molnar, P. (1979), Earthquake recurrence intervals and plate tectonics, *Bulletin of the Seismological Society of America*, *69*(1), 115-133.

Morishita, Y., M. Lazecky, T. J. Wright, J. R. Weiss, J. R. Elliott, and A. Hooper (2020), LiCSBAS: An Open-Source InSAR Time Series Analysis Package Integrated with the LiCSAR Automated Sentinel-1 InSAR Processor, *Remote Sensing*, *12*(3), 424.

Nocquet, J.-M. (2012), Present-day kinematics of the Mediterranean: A comprehensive overview of GPS results, *Tectonophysics*, *579*, 220-242.

Pagli, C., H. Wang, T. J. Wright, E. Calais, and E. Lewi (2014), Current plate boundary deformation of the Afar rift from a 3-D velocity field inversion of InSAR and GPS, *Journal of Geophysical Research: Solid Earth*, *119*(11), 8562-8575.

Parsons, B., T. Wright, P. Rowe, J. Andrews, J. Jackson, R. Walker, M. Khatib, M. Talebian, E. Bergman, and E. R. Engdahl (2006), The 1994 Sefidabeh (eastern Iran) earthquakes revisited: new evidence from satellite radar interferometry and carbonate dating about the growth of an active fold above a blind thrust fault, *Geophysical Journal International*, *164*(1), 202-217.

Prats-Iraola, P., R. Scheiber, L. Marotti, S. Wollstadt, and A. Reigber (2012), TOPS Interferometry With TerraSAR-X, *IEEE Transactions on Geoscience and Remote Sensing*, *50*(8), 3179-3188.

Reilinger, R., and S. McClusky (2011), Nubia–Arabia–Eurasia plate motions and the dynamics of Mediterranean and Middle East tectonics, *Geophysical Journal International*, *186*(3), 971-979.

Rollins, C., and J.-P. Avouac (2019), A Geodesy- and Seismicity-Based Local Earthquake Likelihood Model for Central Los Angeles, *Geophysical Research Letters*, *46*(6), 3153-3162.

Rousset, B., R. Jolivet, M. Simons, C. Lasserre, B. Riel, P. Milillo, Z. Çakir, and F. Renard (2016), An aseismic slip transient on the North Anatolian Fault, *Geophysical Research Letters*, *43*(7), 3254-3262.

Savage, J. C., and R. O. Burford (1973), Geodetic determination of relative plate motion in central California, *Journal of Geophysical Research (1896-1977)*, *78*(5), 832-845.

Savage, J. C., W. Gan, and J. L. Svarc (2001), Strain accumulation and rotation in the Eastern California Shear Zone, *Journal of Geophysical Research: Solid Earth*, *106*(B10), 21995-22007.

Schmidt, D. A., and R. Bürgmann (2003), Time-dependent land uplift and subsidence in the Santa Clara valley, California, from a large interferometric synthetic aperture radar data set, *Journal of Geophysical Research: Solid Earth*, *108*(B9).

Shen, L., A. Hooper, and J. Elliott (2019), A Spatially Varying Scaling Method for InSAR Tropospheric Corrections Using a High-Resolution Weather Model, *Journal of Geophysical Research: Solid Earth*, *124*(4), 4051-4068.

Shirzaei, M., R. Bürgmann, and E. J. Fielding (2017), Applicability of Sentinel-1 Terrain Observation by Progressive Scans multitemporal interferometry for monitoring slow ground motions in the San Francisco Bay Area, *Geophysical Research Letters*, *44*(6), 2733-2742.

Smith, B. R., and D. T. Sandwell (2006), A model of the earthquake cycle along the San Andreas Fault System for the past 1000 years, *Journal of Geophysical Research: Solid Earth*, *111*(B1), n/a-n/a.

Stein, S., R. J. Geller, and M. Liu (2012), Why earthquake hazard maps often fail and what to do about it, *Tectonophysics*, *562-563*, 1-25.

Stevens, V. L., and J.-P. Avouac (2016), Millenary Mw > 9.0 earthquakes required by geodetic strain in the Himalaya, *Geophysical Research Letters*, *43*(3), 1118-1123.

Tong, X., D. T. Sandwell, and B. Smith-Konter (2013), High-resolution interseismic velocity data along the San Andreas Fault from GPS and InSAR, *Journal of Geophysical Research: Solid Earth*, *118*(1), 369-389.

Torres, R., et al. (2012), GMES Sentinel-1 mission, *Remote Sensing of Environment*, *120*, 9-24.

Üstün, A., et al. (2015), Land subsidence in Konya Closed Basin and its spatio-temporal detection by GPS and DInSAR, *Environmental Earth Sciences*, *73*(10), 6691-6703.

Walters, R. J., B. Parsons, and T. J. Wright (2014), Constraining crustal velocity fields with InSAR for Eastern Turkey: Limits to the block-like behavior of Eastern Anatolia, *Journal of Geophysical Research: Solid Earth*, *119*(6), 5215-5234.

Walters, R. J., P. C. England, and G. A. Houseman (2017), Constraints from GPS measurements on the dynamics of the zone of convergence between Arabia and Eurasia, *Journal of Geophysical Research: Solid Earth*, *122*(2), 1470-1495.

Wang, H., and T. J. Wright (2012), Satellite geodetic imaging reveals internal deformation of western Tibet, *Geophysical Research Letters*, *39*(7).

Wang, H., T. J. Wright, J. Liu-Zeng, and L. Peng (2019), Strain Rate Distribution in South-Central Tibet From Two Decades of InSAR and GPS, *Geophysical Research Letters*, *46*(10), 5170-5179.

Wei, M., D. Sandwell, and B. Smith-Konter (2010), Optimal combination of InSAR and GPS for measuring interseismic crustal deformation, *Advances in Space Research*, *46*(2), 236-249.

Weiss, J. R., et al. (2019), Illuminating subduction zone rheological properties in the wake of a giant earthquake, *Science Advances*.

Wessel, P., W. H. F. Smith, R. Scharroo, J. Luis, and F. Wobbe (2013), Generic Mapping Tools: Improved Version Released, *Eos, Transactions American Geophysical Union*, *94*(45), 409-410.

Wright, T. (2016), The earthquake deformation cycle, *Astronomy & Geophysics*, *57*, 4.20-24.26.

Wright, T. J., B. Parsons, and E. Fielding (2001), Measurement of interseismic strain accumulation across the North Anatolian Fault by satellite radar interferometry, *Geophysical Research Letters*, *28*(10), 2117-2120.

Wright, T. J., B. E. Parsons, and Z. Lu (2004a), Toward mapping surface deformation in three dimensions using InSAR, *Geophysical Research Letters*, *31*(1), n/a-n/a.

Wright, T. J., B. Parsons, P. C. England, and E. J. Fielding (2004b), InSAR Observations of Low Slip Rates on the Major Faults of Western Tibet, *Science*, *305*(5681), 236-239.

Wright, T. J., J. R. Elliott, H. Wang, and I. Ryder (2013), Earthquake cycle deformation and the Moho: Implications for the rheology of continental lithosphere, *Tectonophysics*, *609*, 504-523.

Xu, X., D. T. Sandwell, and B. Smith-Konter (2020), Coseismic Displacements and Surface Fractures from Sentinel-1 InSAR: 2019 Ridgecrest Earthquakes, *Seismological Research Letters*.

Yu, C., N. T. Penna, and Z. Li (2017), Generation of real-time mode high-resolution water vapor fields from GPS observations, *Journal of Geophysical Research: Atmospheres*, *122*(3), 2008-2025.

Yu, C., Z. Li, and N. T. Penna (2018a), Interferometric synthetic aperture radar atmospheric correction using a GPS-based iterative tropospheric decomposition model, *Remote Sensing of Environment*, *204*, 109-121.

Yu, C., Z. Li, N. T. Penna, and P. Crippa (2018b), Generic Atmospheric Correction Model for Interferometric Synthetic Aperture Radar Observations, *Journal of Geophysical Research: Solid Earth*, *123*(10), 9202-9222.

Zhang, J., Y. Bock, H. Johnson, P. Fang, S. Williams, J. Genrich, S. Wdowinski, and J. Behr (1997), Southern California Permanent GPS Geodetic Array: Error analysis of daily position estimates and site velocities, *J Geophys Res-Sol Ea*, *102*(B8), 18035-18055.